# How boundary slip controls emergent Darcy flow of liquids in tortuous and in capillary pores

Kuldeep Singh*
*Department of Geology, Kent State University, 325 S. Lincoln St., Kent Ohio 44242*

(Received 12 July 2019; revised 8 March 2020; accepted 15 June 2020; published 6 July 2020)

Fundamental investigations of how boundary slip relative to the no-slip condition for liquid flow in a set of two distinct idealized pore geometries, i.e., a diverging-converging tortuous pore, in contrast to a straight tube capillary pore, contribute to emergent Darcy flow and flow enhancement are presented. Using steady-state solutions to Navier-Stokes equations, a sensitivity study investigates the role of (a) a large variation in boundary slip reported in the literature, and (b) a large variation in pore-throat sizes found in geologic porous media. Results show that both the pore geometry and their pore-throat sizes contribute to differences over several orders of magnitude in the emergent Darcy flow behavior and the flow enhancement. Tortuous pores contribute to a lower flow enhancement relative to the capillary pores, and while the larger pore throats (i.e., $\geqslant 10\,\mu$m) negligibly enhance flow, it increasingly becomes significant for the micron-size pore throats. From capillary pores, flow enhancement is found to increases linearly in an unlimited manner with an increment in boundary slip relative to the no-slip condition. In contrast, flow enhancement from diverging-converging tortuous pores is found to get limited defined by an asymptote for flows with a larger boundary slip. Capillary pores offer no change in resistance to flow due to boundary slip. In contrast, the very nature of diverging-converging tortuous pore geometry offers growth in drag forces and energy dissipation rate, i.e., an increase in resistance to flow, which contributes to the asymptote or the limited flow enhancement. A set of theoretical models are presented, which can be used to predict the flow enhancement as a function of boundary slip and spatial-scale of pore throats. This study may have implications for predicting flow enhancement and pressure loss during fluid injection or recovery from low permeability geologic reservoirs, and relevant to other engineering applications, e.g., hydraulics in corrugated channels or design of carbon nanotube membranes for desalinization purposes.

DOI: 10.1103/PhysRevE.102.013101

## I. INTRODUCTION

No-slip boundary condition, which leads to the traditional form of the averaged continuity equation, i.e., $\nabla \cdot \boldsymbol{u} = 0$, is fundamental to the theoretical derivation of Darcy's Law from Navier-Stokes equation [1–3]. Subsequently, the usage of no-slip boundary condition has become a norm for most analytical and numerical studies of fluid flow over a solid surface including pore-scale fluid dynamic studies, with the exception of the gas flow in porous media [4,5].

In last two decades, advances both in computational resources and high-resolution imaging of porous media, in combination, has revolutionized the fundamental investigations of how complex porous structure modify fluid dynamics in three-dimensions (3D) and its dependent transport of dissolved and particulate matter at the pore-scale, which altogether gets manifested as the phenomenon of continuum porous media [3,6]. Most pore-scale fluid dynamics studies, which use direct numerical simulation solving Navier-Stokes equations, or the lattice Boltzmann method, or solution of Hagen-Poiseuille equation used in pore-network modeling, continue to implement the no-slip boundary condition [5,7–10]. The results from pore-scale studies are often used to benchmark results of laboratory experiments and predict flow and transport phenomena of the field scale [11–14].

In contrast, the liquid slip at liquid-solid interface/boundary i.e., the velocity of a liquid at the boundary $\neq 0$, is a well-known phenomenon [15–19]. The liquid slip also known as viscous slip or Navier slip arise due to weak van der Waals interactions at the liquid-solid boundary, and is implemented as a slip boundary with a prescribed slip length ($b$), i.e., length past the boundary at which linear extrapolation of velocity profile satisfy the no-slip boundary condition. This results in a liquid velocity at the boundary known as the slip velocity.

The slip length ($b$) spanning from 8 nm to 10s of mm, i.e., several orders of magnitude larger than the length scale of confinement, have been reported from laboratory experimental studies and molecular dynamics (MD) simulations [18,20,21]. The large variations in slip length exist as a function of wettability [18,20,22], surface roughness [23–25], and shear rate [26,27]. For example, from laboratory experiments, slip length of 8–9 nm was found on perfectly wetting mica and glass surfaces, i.e., contact angle, $\theta = 0$ [28], $b$ of $\sim$50 nm was found from 10-μm-deep hydrophilic glass microchannel [29], $b$ of 85 nm was found from rough hydrophilic glass surface [30], and a large $b$ of $\sim$70 μm is inferred from reported slip velocity of 0.01 (m/s) from 14-mm-diameter hydrophilic glass tube [31]. Likewise, large slip lengths of 0.1 to $\sim$10 μm are reported from hydrophobic glass surfaces [29,32], slip

*Corresponding author: ckuldeep@kent.edu

 

lengths of 20 to ∼200 μm are found from rough-patterned superhydrophobic surfaces [22,33,34], and $b$ of up to 68 mm was found from 7-nm carbon nanotube [21]. Using MD simulation, slip lengths between 0.1 and 80 μm were computed for a series of hydrophilic to hydrophobic surfaces, respectively [20].

Aquifer/reservoir minerals are known to exhibit large variations in wettability and surface roughness, which can be similar in form to patterned superhydrophobic surfaces, for example, the surface roughness of up to 1 μm is reported from quartz grains [35]. Wettability of aquifer/reservoir minerals generally exhibits strong to weak wetting characteristics [36,37] that can transform to mixed-wet or hydrophobic characteristics due to aging from organic acids found in soils or hydrocarbon reservoirs [38,39]. The effect of slip flow can be insignificant when slip length is smaller than pore-throat sizes, however, slip flow may significantly modify the flow field when $b$ is greater than pore-throat sizes. Pore-throat sizes for most aquifers, reservoirs, and soils (excluding clay-rich formations, e.g., Shale) span between 0.1 and 100 μm [40]. At what wettability or slip lengths or pore-throat sizes do aspects of slip flow become significant? Specifically, among pore-scale fluid dynamic studies, how liquid slip flow, which is likely related to the wettability of porous media, modify Darcy flow behavior, has not been well studied. Aspects of such a study bear implication for improving the predictive nature of pore-scale models, and thus aid in representative upscaling of the pore-scale phenomenon.

In this paper, the main questions addressed are *how does the boundary slip during liquid flow in pores modify the emergent Darcy flow and permeability*? *How do different pore-throat sizes in the combination of a large variation in slip length, as reported in the literature, contribute to the emergent Darcy flow and permeability*? and finally, *are there any differences in the modification of emergent flow behavior between straight tube capillary vs tortuous pores*? To address these related questions, a series of diverging-converging tortuous and straight tube capillary pores, representative of pore-throat sizes spanning $10^{-7}$ m to $10^{-4}$ m are designed. Using steady solutions to Navier-Stokes equations, a sensitivity study is conducted by varying wall boundary conditions from no-slip to slip boundary with a range of slip lengths spanning between $10^{-9}$ and $10^{-4}$ m, i.e., as reported in the literature. The methods section (II.) describes the details of pore geometry design and the solution scheme of Navier-Stokes equations with the implementation of slip boundary conditions. Next, the evaluation of computed flow fields, related findings, and development of theoretical models are presented in Sec. III. The examination of physical mechanisms, e.g., resistive forces and energy dissipation, which contribute to the observed findings and related discussions are presented in Sec. IV. Finally, Sec. V. presents a summary.

## II. METHODS

### A. Pore-scale tortuous vs capillary pore geometry design, and motivation

To study the aspects of tortuous flow around sediment grains of porous media, in contrast to studying pore-scale flow using the straight tube capillary pore geometry, i.e., the framework for a capillary bundle or the pore-network modeling, a series of axis-symmetric diverging-converging pores, which represent 3D channel flow around sediment grains, in combination with a series of axis-symmetric straight tube capillary pores are designed for this study [Figs. 1(a)–1(c).

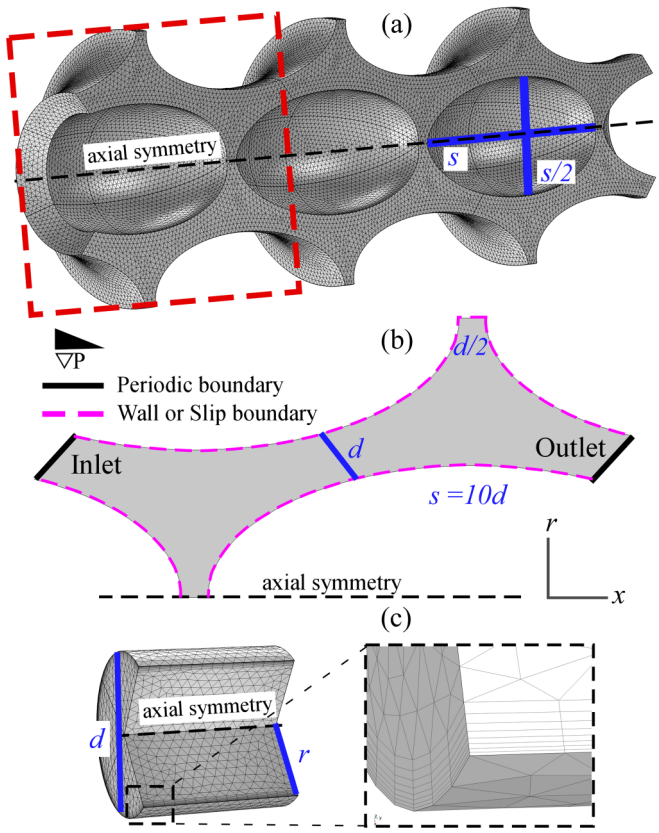


FIG. 1. A cut section from a 3D rendition of an axis symmetric periodic tortuous pores composed of periodic array of three pore units (red dashed square highlights a single pore unit), which are formed around staggered arrangement of sediment grains of size $s$, (b) 2D section of a single tortuous pore unit showing anisotropic pore throats of diameter ($d$) and boundary conditions, and (c) A cut section from a 3D rendition of an axis symmetric capillary pore.

In an attempt to design tortuous pore geometries representative of natural porous media, i.e., a media which display hydraulic anisotropy due to compaction related to geologic burial processes, a series of compacted sediment grains, i.e., grains with aspect ratios of 1:2 in $r$ and $x$ directions, respectively [$s$; Fig. 1(a)], are arranged in a staggered pattern. The spacing between the grains is optimized to obtain hydraulic anisotropy by arranging pore-throat sizes ($d$) in a ratio of 1:2 in $r$ and $x$ directions, respectively [$d$; Fig. 1(b)]. Here, the $x$ coordinate is the primary direction of flow, and $r$ is the radial coordinate of the axis-symmetric plane. In this specific design, the sediment grain sizes are 10 times the pore-throat sizes in each specific direction [i.e., $s = 10d$; Fig. 1(b)]. This ratio is similar to average pore-throat to grain sizes found in natural porous media [14,40–42]. The resulting pore spaces around sediment grains form a channel of tortuous pores i.e., a channel with a geometric tortuosity of 1.22, which represents a more realistic diverging-converging tortuous pore geometry,

is homogeneous, but with a moderate amount of anisotropy. Similar pore geometries of grain packs have been used as benchmarks for studying flow and transport phenomena of porous media [7].

To compare and contrast the results of this study with other pore-scale studies which rely on either the 1D analytical solution to Navier-Stokes equations or the Hagen-Poiseuille equation or the pore-network modeling which presumes pore channels as a network of straight tubes, a series of axis-symmetric straight tube capillary pores are also designed for this study [Fig. 1(c)]. These capillary pores have a diameter, $d$, similar to the pore-throat diameter of tortuous pores, but with no anisotropy and no diverging-converging geometry, and thus, have a geometric tortuosity of 1.

In natural porous media, pore-throat sizes could vary significantly related to both the depositional environment and the burial history, and the flow enhancement due to boundary slip may manifest differently in different size pores. To account for this large variability found in the size of pore throats, both the tortuous pore and capillary pore domains were isotropically scaled in log-space to obtain $13 \times 2$ domains with their pore-throat sizes, $d$ representing a variation between $10^{-7}$ and $10^{-4}$ m found from fine siltstones to sandstone reservoirs [40].

### B. Computational fluid dynamics, boundary conditions, and numerical scheme

Fluid hydraulics at pore-scale is studied by conducting computational fluid dynamics (CFD) simulations, which involve solving Navier-Stokes and continuity equations, numerically using the finite element method (FEM). Single-phase steady incompressible fluid flow in pore domains is governed by

$$\nabla \cdot p\mathbf{I} = \nabla \cdot \mu\,(\nabla \boldsymbol{u} + (\nabla \boldsymbol{u})^{\mathrm{T}}) - \rho(\boldsymbol{u} \cdot \nabla)\boldsymbol{u}, \tag{1}$$

$$\nabla \cdot \boldsymbol{u} = 0, \tag{2}$$

where $\rho$ is the fluid density, $\boldsymbol{u} = [u, v]$ is a velocity vector with components in $r$ and $x$ directions, respectively, $\mu$ is dynamic viscosity and $p$ is total pressure. Standard properties of water, i.e., $\rho = 1000\,\mathrm{kg\,m^{-3}}$, and $\mu = 0.001$ (Pa s) are used. A pressure gradient, $\nabla p = 1(\mathrm{Pa\,m^{-1}})$ is applied across the periodic inlet-outlet boundaries [Fig. 1(b)], which allow both for the flow to be fully developed at the inlet, and flow from a single pore domain to be representative of flow from an infinitely long pore channel in the $x$ direction, i.e., the main direction of flow. The applied pressure gradient results in a laminar flow regime with Reynolds number, $\mathrm{Re} < 1$. The Reynolds number, Re, is calculated as

$$\mathrm{Re} = \frac{\rho\, U_a\, d}{\mu}, \tag{3}$$

where, $U_a$ is average velocity in the $x$ direction, and $d$, the pore-throat diameter is the characteristic length.

All pore boundaries, i.e., wall [Fig. 1(b)] are considered at first with a prescribed no-slip boundary condition, i.e, the velocity at the boundary, $\boldsymbol{u}_b = 0$. And, to study the role viscous boundary slip, a slip boundary condition, i.e., velocity, $\boldsymbol{u}_b > 0$ at the boundary i.e., the wall [Fig. 1(b) is implemented by

$$\boldsymbol{u}_b = \frac{b}{\mu}\boldsymbol{\tau}, \tag{4}$$

where $b$ is the prescribed slip length and $\boldsymbol{\tau}$ is shear stress. Given that there exists a large variability in reported slip lengths in literature which is likely related to the nature of wettability of media, a sensitivity study is conducted by systematically varying the slip length, $b$ between $10^{-9}$ and $10^{-4}$ m. Steady-state numerical solutions to Navier-Stokes and continuity equations are computed by applying a periodic pressure drop, and a no-slip boundary condition. Next, a series of simulations are conducted on $13 \times 2$ pore domains by prescribing ten different values of slip length per one log decade, which together lead to a total of 1352 computational simulations considered in this study.

Finite element mesh sensitivity to the computed flow fields with large variances in $b$ and $d$ is conducted by introducing boundary layer elements, which are a subset of FEM meshing methods. The usage of boundary layer elements allow a high-resolution mesh refining parallel to boundaries or the wall of pore domains [Fig. 1(c)], and thus, enables us to accurately resolve the physics of the boundary layer, e.g., shear stress, $\boldsymbol{\tau}$ on the boundary. The mesh sensitivity based on the absolute change in velocity, i.e., $|\Delta \boldsymbol{u}| \leqslant 10^{-4}$ (m/s) or 99.99% accuracy in velocity approximation resulted in $\sim 4 \times 10^6$ elements for the 2D sections of axis-symmetric tortuous pores. Numerical solutions to Eqs. (1)–(3) are conducted using the finite element based CFD module of Comsol Multiphysics software. The numerical solution scheme included the implementation of a higher order, i.e., quadratic Lagrange shape functions for $\boldsymbol{u}$ and $p$, which allow for improved numerical accuracy with a trade-off to an increase in the computational time. The steady solutions were computed using a direct Multifrontal massively parallel sparse solver .

## III. RESULTS

### A. Flow field, Darcy's law, and permeability

The CFD simulations provide the flow field from tortuous and capillary pores which form the basis for evaluating their effective hydraulic characteristics. The periodic nature of pores used here, allow its single pore unit to outline the representative elementary volume, which may, however, need redefinition for including heterogeneity found at a larger length scales. Evaluation of the computed flow fields at pore scale allows us to recover Darcy's law which is similar in ways to the derivation of Darcy's law from Navier-Stokes Eqs. (1) and (2). In this study, the computed relationship between pressure gradient and volumetric flux from the outlet, which follows Darcy's Law, is used to calculate the permeability, $k$ [43,44]. Darcy's Law is

$$\frac{Q}{A} = q = -\frac{k}{\mu}\nabla p, \tag{5}$$

where, $Q$ is volumetric flux ($\mathrm{m^3/s}$) obtained by integrating the magnitude of $\boldsymbol{u}$, i.e., $U$ over the outlet boundary, $A(\mathrm{m^2})$ is the area of cross section of the outlet boundary, $q$ is Darcy flux (m/s), and $k(m^2)$ is the permeability. Similar to $q$, the average $U$, i.e., $U_a$ is $= Q/A$.

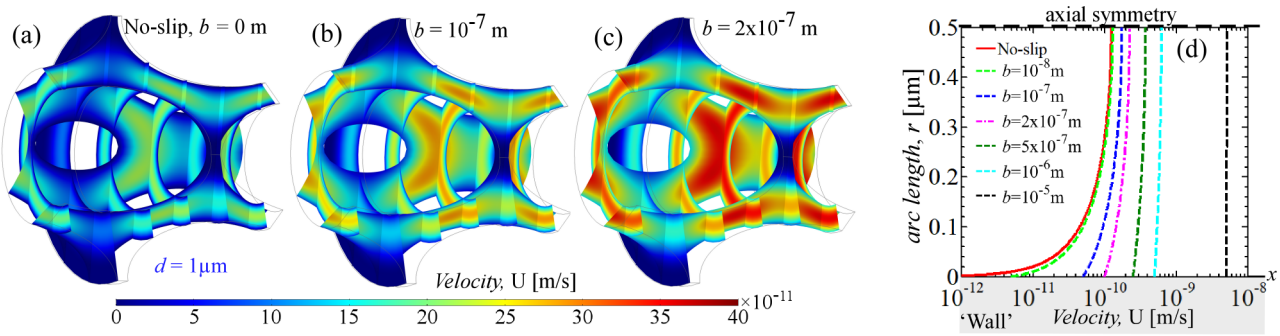


FIG. 2. Orthogonal cross-sectional slices of computed velocity fields from a tortuous pore ($d = 1$ μm) showing evolution of velocity within a pore as a results of no-slip to slip boundary conditions (a)–(c), and (d) computed velocity profiles from a half section of an axis symmetric capillary pore ($d = 1$ μm) as a result of different slip lengths ($b$).

The computed steady-state flow fields from the diverging-converging tortuous pore ($d = 10^{-6}$ m) show differences in how velocity gets enhanced within different sections of a pore as a result of changes in the boundary slip [Figs. 2(a)–2(c)]. With an increase in boundary slip, i.e., the change from a no-slip to a stepwise increase everywhere on the boundary/wall, velocity enhancement gets focused near pore throats with negligible changes in the pore body [i.e., wider region away from pore throats; Figs. 2(a)–2(c)]. For example, near the boundary of pore throats with $d = 10^{-6}$ m, an increase in velocity of up to $10^2$ (m/s) can be found related to $10^2$ (m) increase in slip length, whereas negligible changes in velocity are found within the dead-end part of the pore [Figs. 2(a)–2(c)].

In comparison, the computed steady-state flow fields from the capillary pore ($d = 10^{-6}$ m) show a relatively consistent velocity enhancement everywhere with an increase in the boundary slip. While velocity enhancement at the boundary of a capillary pore is always proportional to the slip length, velocity enhancement in the middle of capillary pore transitions from a negligible change during partial or small boundary slip (i.e., $b \leqslant 10^{-8}$ m) to a change proportional to the change in boundary slip when it is on the same order as the diameter of the capillary pore. The latter can be better observed from Fig. 2(d), which shows velocity profiles for different slip lengths $b$ from a half-section of the capillary pore. With an increase in boundary slip, velocity profiles transform from a large velocity variation in the parabolic profile to negligible variations, which appears as a characteristic plug-flow profile in a semilog plot [Fig. 2(d)].

These observed variations of how and why velocity changes differently within a pore as a function of pore geometry and boundary slip, and how such velocity variations within a pore gets manifested as the effective hydraulic behavior of porous media are the main objectives of investigations presented in this paper.

### B. Evolution of effective hydraulic behavior with boundary slip

To evaluate the variations in effective permeability of straight tube capillary and diverging-converging tortuous pore geometries, the results are presented in two different ways, first, variations in permeability are presented as a function of pore throats sizes (Fig. 3), and later, as a function of slip length (Fig. 4).

#### *1. Capillary pores*

Computed permeability, $k$ as a function of pore throat ($d$) with the no-slip condition in capillary pores, follows the Hagen-Poiseuille law, i.e., $k \propto d^2$ [Fig. 3(a)]. With a small increase in boundary slip from the no-slip condition (i.e., when $b < 10^{-6}$ m), the pore throats with the smallest sizes exhibit the most important deviation from $k \propto d^2$, however, for larger sizes this deviation declines and the permeability tends to follow the Hagen-Poiseuille law [Fig. 3(a)]. For flows with a large boundary slip (i.e., $b > 10^{-5}$ m), the variations in $k$ are found to be a linear function of $d$ for all size pore throats, i.e., the exponent 2 in Hagen-Poiseuille law ($k \propto d^2$) is found to change from 2 to 1 [Fig. 3(a)].

From another perspective [Fig. 4(a)], the computed permeability, $k$ as a function of boundary slip $b$ (i.e., from $b = 0 \rightarrow b = 10^{-9}$ m to $b = 10^{-4}$ m) for various size pore throats shows that there are negligible changes with a small increase in the boundary slip from the no-slip condition (i.e., when $b \ll d$), which, however, transition to a linear increase in the permeability, i.e., $k \propto b^1$ for a relatively large increase in the boundary slip (i.e., when $b \gg d$). This transition from negligible changes to a linear increase is found to appear when the magnitude of slip length is on the same order as the size of pore throats, i.e., when $b \approx d$ [Fig. 4(a)].

#### *2. Diverging-converging tortuous pores*

With the no-slip condition, the permeability variation as a function of pore-throat diameter $d$ of tortuous pores, is also found to follow the Hagen-Poiseuille law, i.e., $k \propto d^2$ [Fig. 3(b)]. And, with small increases in boundary slip (i.e., when $b < 10^{-6}$ m), similar to findings from capillary pores, the pore throats with the smallest sizes exhibit the most important deviation from $k \propto d^2$, however, for larger pore-throat sizes this deviation declines and the permeability tends to follow the Hagen-Poiseuille law [Fig. 3(b)]. Unlike capillary pores, for boundary conditions with a larger slip length, (i.e., when $b > 10^{-5}$ m), the permeability variation with pore-throat diameter tend to once again follow the Hagen-Poiseuille law, i.e., $k \propto d^2$ [Fig. 3(b)]. This indicates

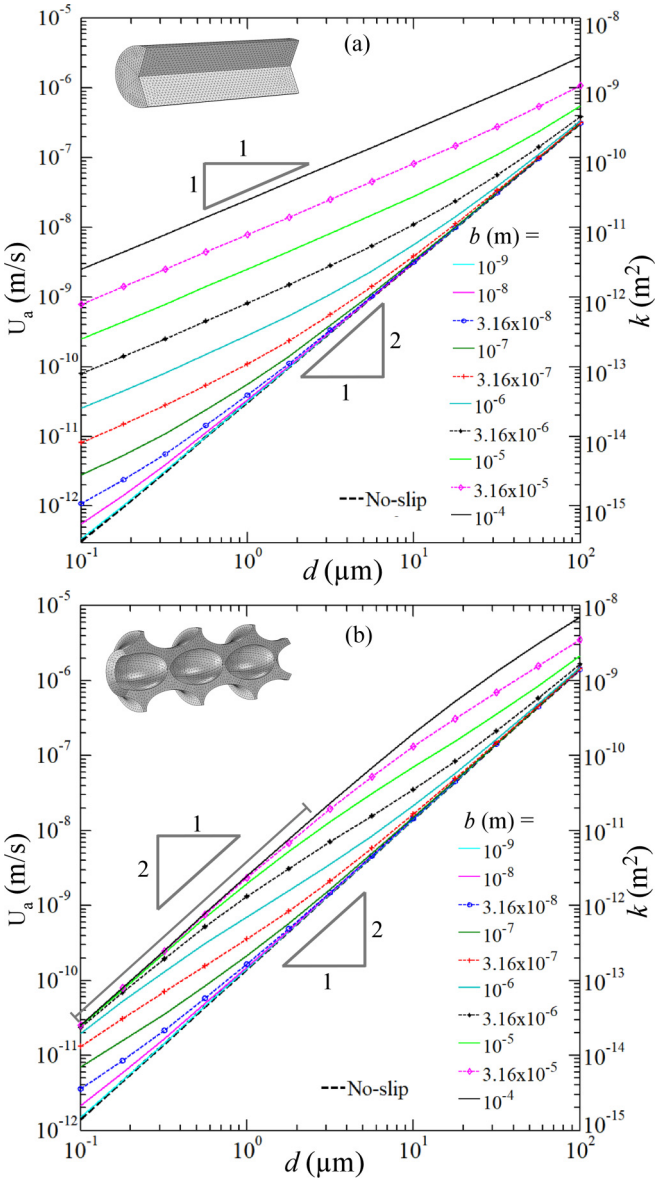


FIG. 3. Average velocity ($U_a$) and permeability ($k$) of various size of pore throats ($d$) as a function of boundary slip, i.e., slip length, ($b$), from capillary (a) and tortuous (b) pores.

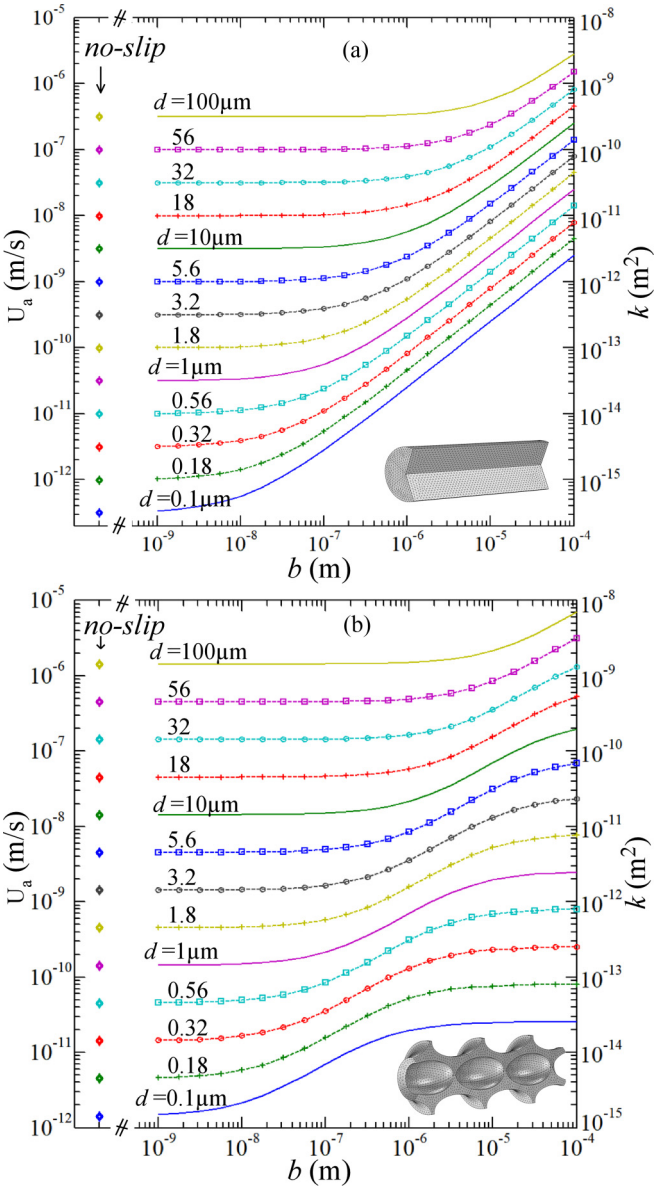


FIG. 4. Average velocity, $U_a$ and permeability, ($k$) as a function of boundary slip, ($b$) for various size pore throats ($d$), of capillary (a) and tortuous (b) pore domains.

that Hagen-Poiseuille law holds for a very large boundary slip in tortuous pores. In contrast, for a system of capillary pores, the permeability with a large boundary slip follows the dependence $k \propto d^1$ [Fig. 3(a)].

From another perspective [Fig. 4(b)], the computed permeability, $k$ of diverging-converging tortuous pores as a function of boundary slip $b$ for various size pore throats, also show that there are negligible changes with a small increase in the boundary slip from the no-slip condition (i.e., when $b \ll d$). However, with a larger boundary slip (i.e., when $b \ll d$), unlike the unlimited linear increase in flow found from capillary pores, the linear increase in permeability of tortuous pores is found to get limited marked by an asymptote in $k$ [Fig. 4(b)]. The boundary slip condition around which the asymptote in $k$ occurs is found to be dependent on the size of pore throats [Fig. 4(b)]. This asymptote which takes on the S-type characteristics curve in log space marks a limited nature of velocity enhancement found from the diverging-converging tortuous pore geometry as opposed to an unlimited velocity enhancement found from the straight tube capillary type models.

### C. Characteristics of flow enhancement due to boundary slip

The impact of an increase in boundary slip from the no-slip condition generally results in an increase in the average velocity or the permeability. The net increase in permeability, i.e., the change in permeability relative to when the no-slip boundary condition is considered, is referred to as the flow enhancement ($E$). The flow enhancement can be

evaluated in the form of arelative factor or a fractional factor defined as

$$E_1 = \frac{k_{(\text{slip})} - k_{(\text{no-slip})}}{k_{(\text{no-slip})}}, \tag{6}$$

$$E_2 = \frac{k_{(\text{slip})}}{k_{(\text{no-slip})}}, \tag{7}$$

where $k_{(\text{no-slip})}(\text{m}^2)$ and $k_{(\text{slip})}(\text{m}^2)$ is permeability with the no-slip and a slip boundary condition, respectively. $E_1$ and $E_2$ are the relative and fractional flow enhancement factors, respectively. Here, $E_2$ is specifically defined to contrast the results from this manuscript with that of in literature. However, $E_1$ may be a more informative metric to examine flow enhancement. Both $E_1$ and $E_2$ distinguish unique characteristics of the emergent flow enhancement behavior, and thus, the usage of the two is justified.

$E_1$ and $E_2$ allow us to evaluate the magnitude of change in permeability as a result of an increase in boundary slip from the no-slip condition. The usage of $E_1$ over the conventional $E_2$ can better examine the flow enhancement due to partial boundary slip. To illustrate the usage of $E_1$, 2D and 3D maps in Figs. 5 and 6 show how the flow enhancement varies as a function of $b$ and $d$ for capillary and tortuous pores, respectively. $E_1$ and $E_2$ are further used to present the normalized flow enhancement to size variations in pore-throat diameter, i.e., a dimensionless factor $b/d$ is used to evaluate the net flow enhancement from both the capillary pores (Fig. 7) and the diverging-converging tortuous pores (Fig. 8).

#### *1. Capillary pores*

In capillary pores, the flow enhancement as evaluated by the factor, $E_1$, is found to increase linearly in an unlimited manner with an increase in the boundary slip $b$ [Figs. 5(a)]. This can be more clearly noted from the 3D planar surface in Fig. 6(a), and the plot of $E_1$ for a few different size capillary pores [Fig. 7(a)]. This linear relationship found from capillary pores indicates that the flow enhancement can be significantly large, i.e., up to several orders of magnitude; for example, an increase in $E_1 > 10^3$ can be found for a geometry, with $d = 10^{-7}$ m and $b > 10^{-5}$ m (Figs. 5 and 6). However, how much flow enhancement can occur for a given boundary slip depends on the size of capillary pore throats [Figs. 7(a) and 7(b)]. The larger size pore throats (i.e., when $d \gg b$) exhibit an insignificant amount of flow enhancement that tends to become significant when the boundary slip is on the same order or greater than the size of pore throats (i.e., when $b \gtrsim d$). Note that the usage of $E_2$ better distinguishes the differences in the magnitude of flow enhancement with lager boundary slips, whereas the usage of $E_1$ can better distinguish the differences between smaller flow enhancements related to smaller boundary slips [Figs. 7(a) and 7(b)].

The net change in flow enhancement factors both due to boundary slip and the size of pore throats can be further evaluated by using a dimensionless parameter $b/d$. The usage of $b/d$ shows that the relative flow enhancement, $E_1$ is a linear function of $b/d$, and the fractional flow enhancement factor, $E_2$ is insignificant for $b/d < 10^{-1}$, which tend to become significant and increase linearly for $b/d > 10^{-1}$ [Figs. 7(c) and 7(d)]. In summary, the evaluation of flow enhancements from the straight tube geometry capillary pores signifies that the usage of capillary tube models will result in a prediction of flow enhancement or pressure change, which is directly proportional to the amount of boundary slip, i.e., a larger boundary slip will always lead to a larger flow enhancement or a larger pressure loss.

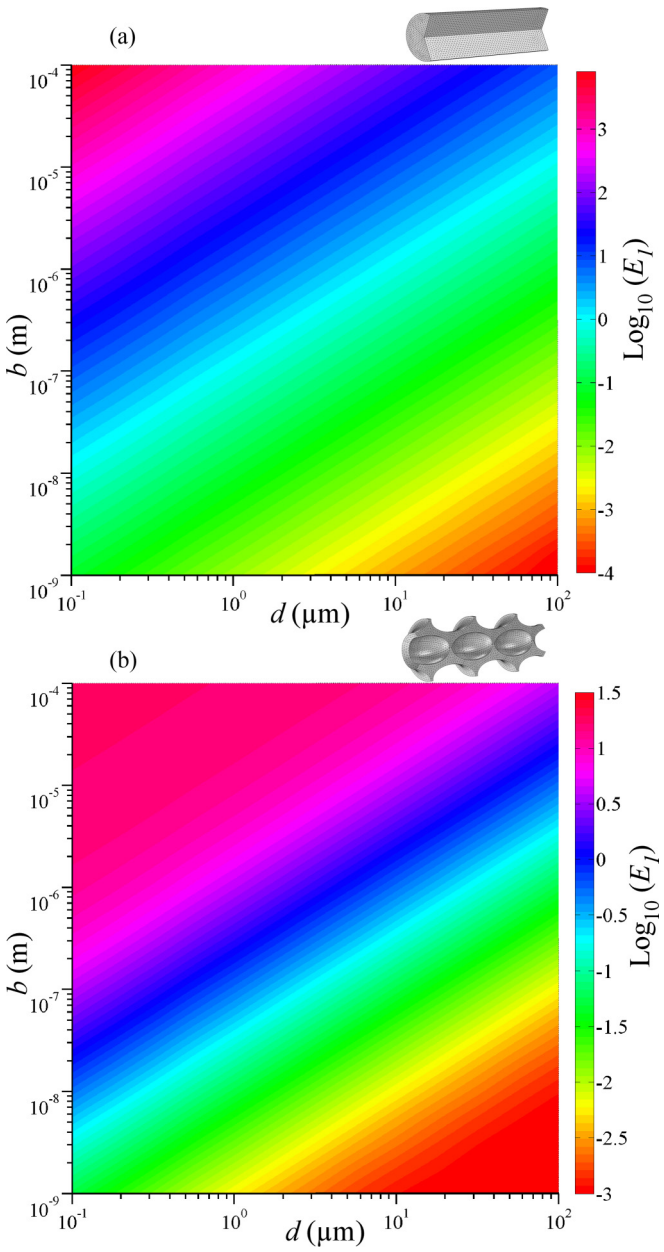


FIG. 5. 2D maps of the flow enhancement factor, $E_1$ as a function of pore-throat size, $d$ and slip length, $b$ from capillary (a) and tortuous (b) pores.

#### *2. Diverging-converging tortuous pores*

The flow enhancement factor, $E_1$ from diverging-converging tortuous pores, similar to capillary pores, also shows a linear increase with an increase in boundary slip when $b < d$ [Fig. 8(a)]. However, this linear relationship,

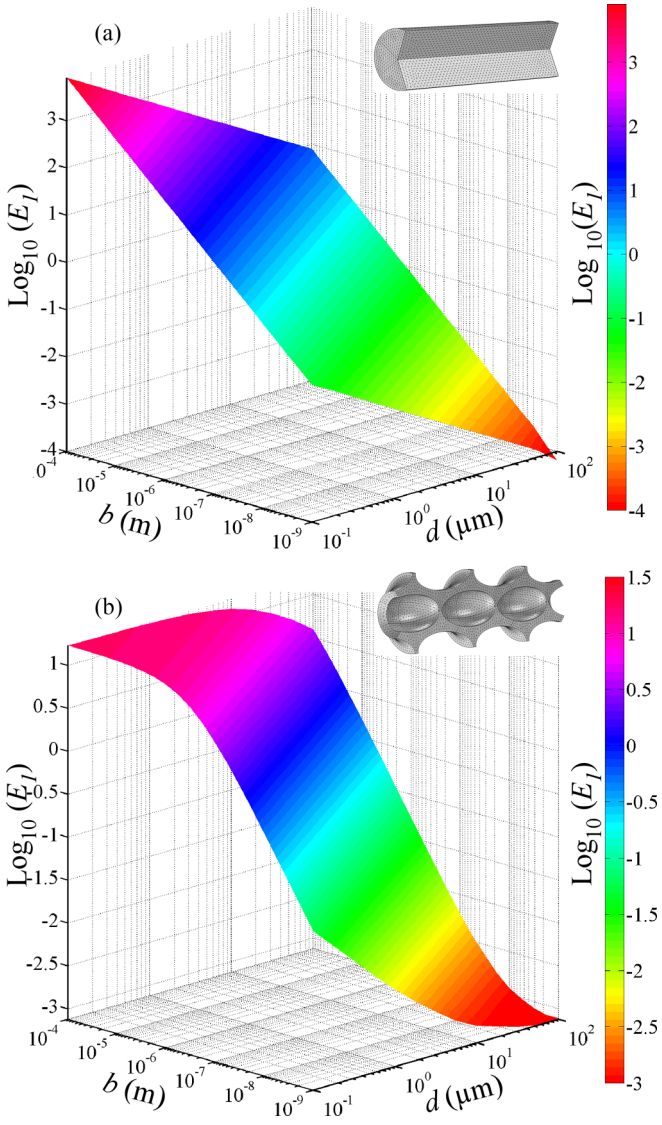


FIG. 6. 3D maps of the flow enhancement factor, $E_1$ showing a planar or linear flow enhancement from capillary pores (a) relative to the limiting flow enhancement behavior found from the tortuous pores (b).

unlike its unlimited character observed from capillary pores, is found to get limited marked by an asymptote for flows with a larger boundary slip relative to the size of pore throats, i.e., when $b > d$ [Figs. 6(b) and 8(a)]. On the other hand, the fractional flow enhancement factor, $E_2$, similar to capillary pores, shows insignificant changes when $b \ll d$, and which tend to a linear relationship when $b < d$ to $b \sim d$. And, in contrast to capillary pores and as also noted from $E_1$ of tortuous pores, this linear relationship gets get limited marked by an asymptote when $b > d$. This limited character of the fractional flow enhancement factor with variations in boundary slip can be observed as the S-type characteristic curve in Fig. 8(b). This asymptote or the S-type characteristic defines that the maximum amount of flow enhancement is limited to $10^{1.23}$ or a factor of 17 for all scenarios considered.

The net change in flow enhancement factors both due to boundary slip and the size of tortuous pores can also be evaluated by using a dimensionless parameter $b/d$. Here, $E_1$ shows that the linear increase tends to asymptote for $b/d \sim 1$ and remains unchanged for $b/d > 10$ [Fig. 8(c). And, similar to capillary pore, $E_2$ outlines that there is negligible flow enhancement when $b/d < 10^{-1}$ and which tend towards a linear increase for $b/d > 10^{-1}$. However, as also noted from $E_1$, the flow enhancement factor, $E_2$ tends to asymptote for $b/d \sim 1$ and remains unchanged for $b/d > 10$ [Fig. 8(d). In summary, the flow enhancement factors show that the geometry of pore and pore throats has a vital control, on how liquid slip flow manifests as the emergent Darcy flow (Figs. 5 and 6), an aspect that has been overlooked so far.

This study finds that with the representation of pore-scale porous media by a straight tube capillary geometry as opposed to a more realistic diverging-converging tortuous pore geometry, upscaling of related hydraulic parameters associated with the boundary slip, will contribute to over predicting flow enhancement, flow rate, and pressure drop by several orders of magnitude, an aspect critical, for example, for evaluating the efficiency and integrity of either waste storage or energy recovery processes from geologic reservoirs. Likewise, this study may bear implications for many other engineering applications, for example, evaluation of accurate slip lengths from tortuous nanomicro channels, hydraulics in corrugated channels, and design of carbon nanotube (CNT) membranes for desalinization purposes.

### D. Theoretical models to predict flow enhancement due to boundary slip

Fluid flow in a capillary pore with the no-slip boundary condition is given by the Hagen-Poiseuille (HP) equation:

$$Q_{HP} = \frac{\pi\, r^4}{8\,\mu}\,\frac{\Delta \mathrm{P}}{L}, \tag{8}$$

where, $Q_{HP}$ is volumetric flux with the no-slip boundary condition, $r$ is the radius of the capillary pore. Here, $r = d/2$ and $L$ is the length of the pore. From Eq. (8), $r^2/8\mu$ is $k_{(\mathrm{no-slip})}$ . For a slip boundary condition with a prescribed slip length ($b$), fluid flow in a capillary pore is given by a modification to the Hagen-Poiseuille equation [45]:

$$Q_{\mathrm{slip}} = Q_{HP}\left(1 + 4\,\frac{b}{r}\right), \tag{9}$$

where $Q_{\mathrm{slip}}$ is volumetric flux with a slip boundary condition of slip length, $b$. Using Eqs. (8) and (9) in combination with the definition of Eqs. (6) and (7), respectively, flow enhancement factors $E_{1P}$ and $E_{2P}$ can be calculated as

$$E_{1P} = 4\,\frac{b}{r}, \tag{10}$$

$$E_{2P} = 1 + 4\,\frac{b}{r}, \tag{11}$$

where, the subscript $P$ in $E_{1P}$ and $E_{2P}$ refers to the capillary pore or the pipe geometry and the subscripts 1 and 2 refer to the type of flow enhancement factor after Eqs. (6) and (7).

Fluid flow in a diverging-converging tortuous pore, i.e., flow through a system of pore-throat and pore body with a

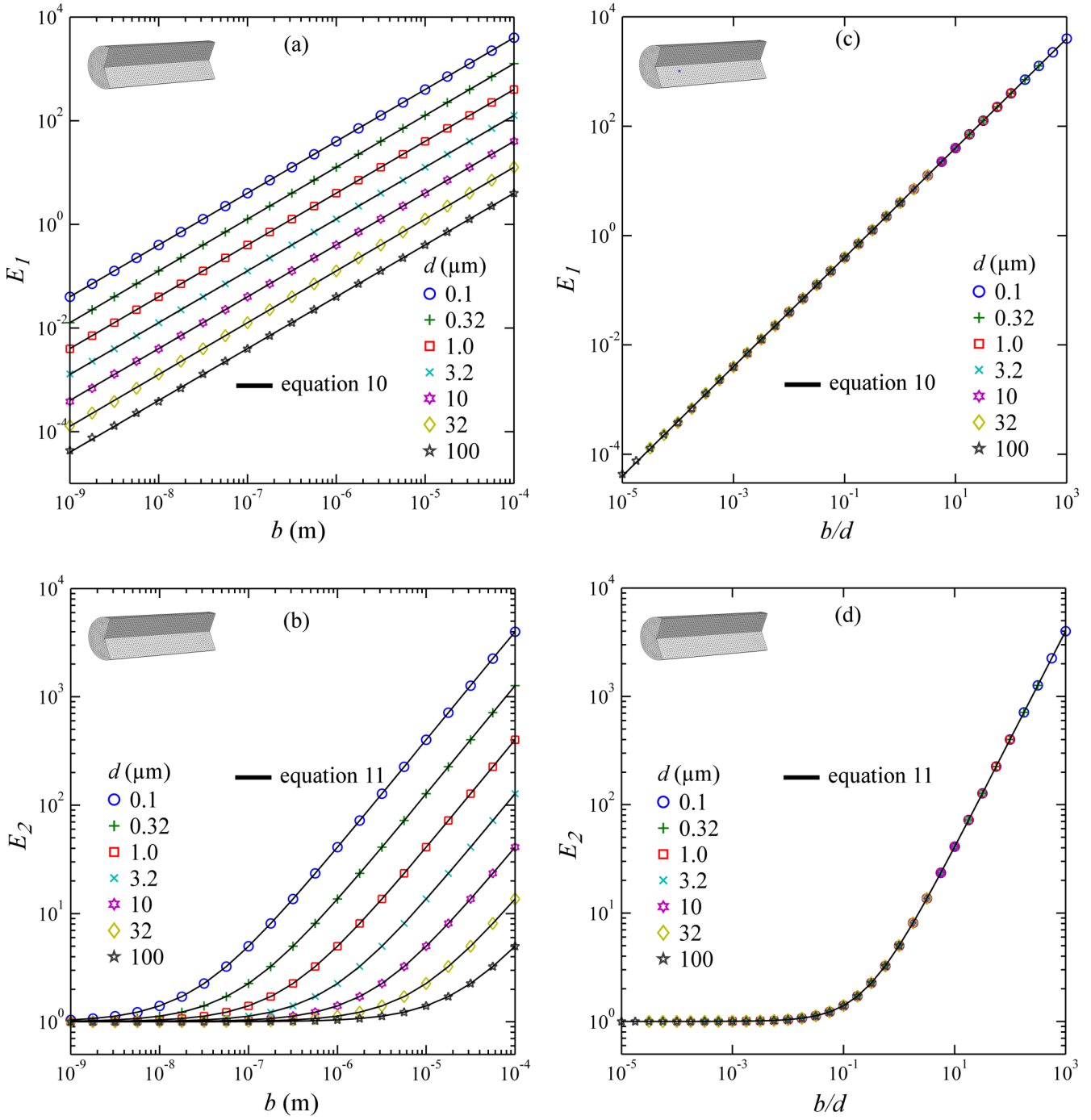


FIG. 7. Flow enhancement computed data ($E_1$ and $E_2$) from straight tube capillary pores and the plots of theoretical Eqs. (10) and (11) which can predict flow enhancement due to boundary slip for various size ($d$) pore throats as a function of slip length $b$ (a) and (b), and as a function of nondimensional parameter $b/d$ (c) and (d). Note: the frequency of total number of domains with various pore-throat sizes have been subsampled to present clarity in figures.

circular cross-section and with the no-slip boundary condition is given after [46,47] as

$$Q_{\text{no-slip}} = \Delta \text{P} \left( \frac{8\mu L}{\pi\, r^4} + \frac{C\,\mu}{r^3} \right)^{-1}, \tag{12}$$

where, $Q_{\text{no-slip}}$ is volumetric flux at the outlet boundary of a diverging-converging tortuous pore and $C$ is a constant with a value of 3 for small length pore throats [46,48]. Note that Eq. (12) was derived by Weissberg [46] for the sharp diverging geometries also known as the end-effects of tubes and can be used here due to the continuity Eq. (2) and mirror symmetry of the diverging to converging pore geometry (Fig. 1). Fluid flow with the boundary slip from a diverging-converging tortuous pore, i.e., a geometry that has a thin pore-throat that diverges to a larger pore body with a circular cross-section can be

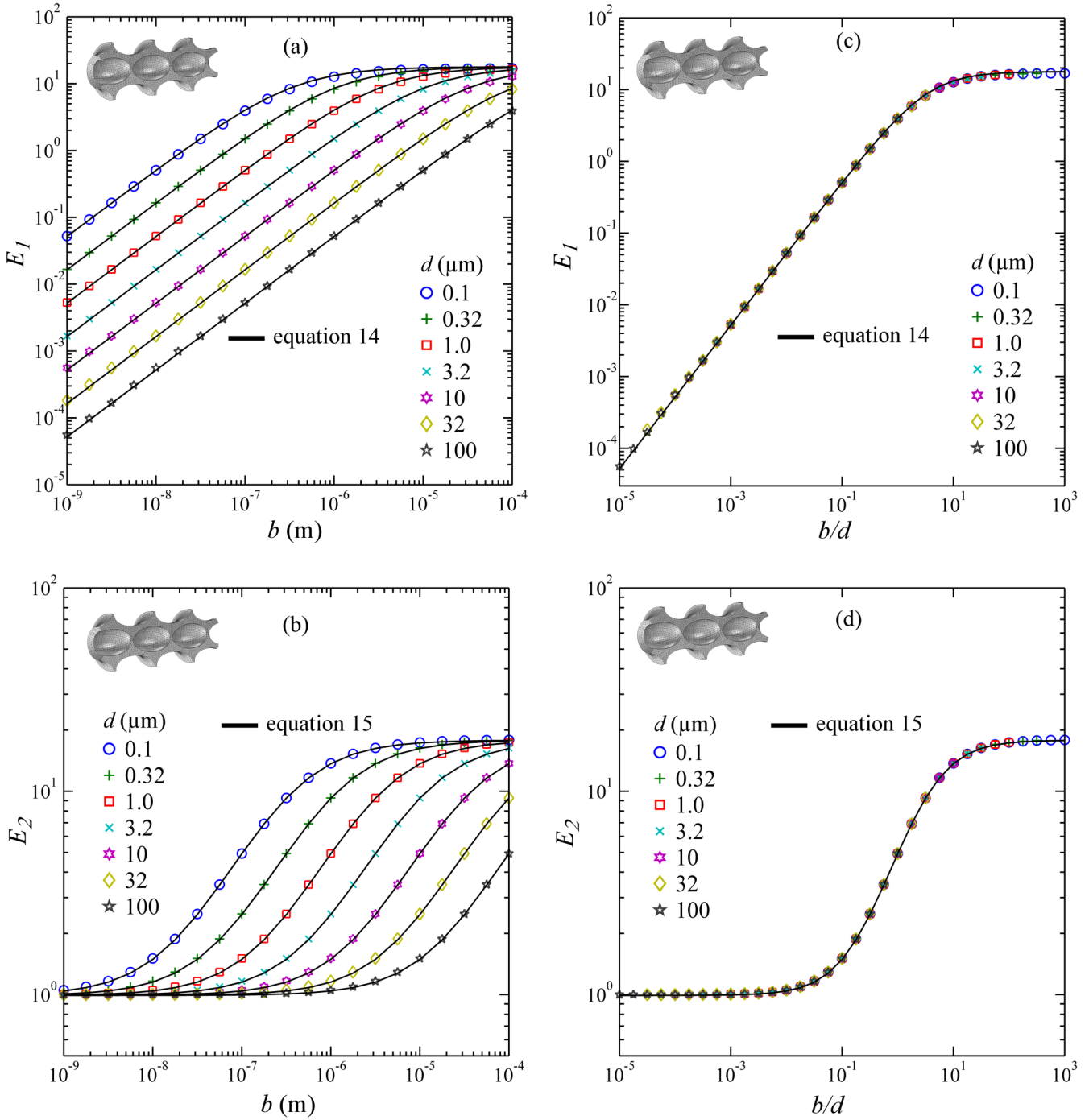


FIG. 8. Flow enhancement computed data ($E_1$ and $E_2$) from diverging-converging tortuous pores and the plots of theoretical Eqs. (14) and (15), which can predict flow enhancement due to boundary slip for various size ($d$) pore throats as a function of slip length $b$ (a) and (b), and as a function of nondimensional parameter $b/d$ (c) and (d). Note: the frequency of total number of domains with various pore-throat sizes have been subsampled to present clarity in figures.

calculated after [49] as

$$Q_{\text{slip}} = \Delta \text{P} \left( \frac{8\mu L}{4\pi r^3 b + \pi r^4} + \frac{C\mu}{r^3} \right)^{-1}, \tag{13}$$

where $Q_{\text{slip}}$ is the volumetric flux of a diverging-converging tortuous pore with a slip boundary condition defined by the slip length $b$. $C$ is the constant same as in Eq. (12). Using the Eqs. (12) and (13) in combination to the definition of Eqs. (6) and (7), respectively, flow enhancement parameters $E_1$ and $E_2$ for the diverging-converging tortuous pore, i.e., $E_{1T}$ and $E_{2T}$ can be calculated as

$$E_{1T} = \left( \frac{1}{4\frac{b}{r}} + \frac{C\pi}{8\frac{L}{r}} \right)^{-1}, \tag{14}$$

$$E_{2T} = \left( \frac{1}{1 + 4\frac{b}{r}} + \frac{C\pi}{8\frac{L}{r}} \right)^{-1}, \tag{15}$$

wherethe subscript $T$ in $E_{1T}$ and $E_{2T}$ refers to the diverging-converging tortuous geometry and the subscripts 1 and 2 refer to the type of flow enhancement factor after Eqs. (6) and (7).

The theoretical Eqs. (10) and (11) can be used to predict the flow enhancement factors $E_{1P}$ and $E_{2P}$, respectively. Figure 7 shows the plot of computed $E_1$ and $E_2$ from the straight tube capillary pore geometry for a variety of pore diameters. Here, the theoretical Eqs. (10) and (11) match with computed $E_1$ and $E_2$ shown for a variety of pore diameters [Figs. 7(a) and 7(b)], and likewise, for the case of dimensionless length $b/d$ [Figs. 7(c) and 7(d)].

Similarly, the theoretical Eqs. (14) and (15) can be used to predict the flow enhancement factors $E_{1T}$ and $E_{2T}$, respectively for the diverging-converging tortuous domains. Figure 8 shows the plot of computed $E_1$ and $E_2$ from the tortuous geometries for a variety of pore sizes. And, the theoretical Eqs. (14) and (15) fit well to the computed $E_1$ and $E_2$ from a variety of pore sizes [Figs. 8(a) and 8(b)], and likewise, for the case of dimensionless length $b/d$ [Fig. 8(c) and 8(d)]. Here, the match of theoretical Eqs. (14) and (15) to computed flow enhancement factors is achieved with a value of $C = 3$.

## IV. ROLE OF DRAG FORCES AND ENERGY DISSIPATION ON FLOW ENHANCEMENT

Drag or resistive forces offered by the pore wall boundaries are manifested in the permeability of the media [50], and therefore, integral to flow enhancement factors, $E_1$ and $E_2$. Likewise, fluid deformation during its flow due to viscous deformation and structural deformation related to fluid-structure interaction, for example, fluid flow in a diverging-converging pore geometry, contribute to the dissipation of energy. The combined effects of energy dissipation get manifested as the permeability of media [51,52], and thus, integral to flow enhancement factors, $E_1$ and $E_2$ [48]. A detailed investigation of how and if drag forces and energy dissipation may control and explain for the observed differences in flow enhancement between the straight tube capillary pores and the diverging-converging tortuous pores is presented in subsequent sections.

### A. Friction drag and form drag

The two components of the total drag force offered by a pore boundary to fluid flow are friction drag ($\mathrm{F}_\tau$) and form drag ($\mathrm{F_N}$). These forces are also known as viscous drag and pressure drag, respectively, however, the former terminology is used in this manuscript. The friction drag arises from the shear stress caused by the moving fluid at the boundary and offers resistance to flow tangent to the boundary. The form drag arises due to fluid pressure and offers resistance to flow normal to the boundary. For fluid flow in the $x$ direction, the $x$ component of local form drag and local friction drag in cylindrical coordinates are computed as

$$f_{N,x} = -[(P\,\boldsymbol{I}) \cdot \boldsymbol{n_x}], \tag{16}$$

$$f_{\tau,x} = \mu\left[\left(\frac{\partial u}{\partial x} + \frac{\partial v}{\partial r}\right) \cdot \boldsymbol{n_r} + 2\left(\frac{\partial v}{\partial x}\right) \cdot \boldsymbol{n_x}\right], \tag{17}$$

where $\boldsymbol{I}$, is the identity matrix, $u$ and $v$ are velocities in $r$ direction and $x$ direction, respectively, and $\boldsymbol{n_r}$ and $\boldsymbol{n_x}$ are unit normal vectors in the $r$ and $x$ directions, respectively. Note that as per the convention in this study, friction drag on the pore boundary yields negative values in the $+x$ flow direction, and vice versa.

For axis-symmetric pore geometries, the net amount of form drag ($\mathrm{F_N}$) for a given pore geometry is calculated by integrating the $x$ component of the local form drag over the surface boundary of the pore domain [i.e., Wall in Fig. 1(b)] as

$$\mathrm{F_N} = \left|\int f_{N,x} \cdot \boldsymbol{n}\, dA\right|, \tag{18}$$

where $\boldsymbol{n}$ is a unit vector normal to pore boundaries. Similarly, the net amount of friction drag, $F_\tau$ is calculated by integrating the $x$ omponent of the local friction drag over the entire surface of the pore body [i.e., Wall in Fig. 1(b)] as

$$\mathrm{F}_\tau = \left|\int f_{\tau,x} \cdot \boldsymbol{t}\, dA\right|, \tag{19}$$

where $\boldsymbol{t}$ is the unit vector tangent to pore boundaries. Note that, to examine the relatively large differences in friction drag in log space, the magnitude of $\mathrm{F}_\tau$ is calculated, i.e., its absolute value, which, however, by definition is a $-$ve value, i.e., a force in the opposite direction to flow, but presented as a $+$ve value.

#### *1. Capillary pores*

The straight tube geometry of capillary pores contributes to a linear pressure drop between the inlet and outlet boundaries. Therefore, pressure changes only in the direction parallel to the main flow direction (i.e., $x$ direction), and it remains constant in the direction perpendicular to the $x$ direction or normal to the wall boundary. This constant pressure yields a zero pressure gradient normal to the boundaries, which results in a zero form drag ($\mathrm{F_N}$) for all boundary slip conditions. Therefore, the geometry of the straight tube of capillary pores offers no form drag irrespective of either a boundary slip or the no-slip condition. Likewise, the straight tube geometry results in a constant velocity in the main flow direction, as such the gradient in velocity perpendicular to the wall boundary is also constant. This constant gradient in velocity results in a constant friction drag ($\mathrm{F}_\tau$) for all boundary slip conditions [Fig. 9(c)].

#### *2. Diverging-converging tortuous pores*

The computed friction drag ($\mathrm{F}_\tau$) from the tortuous pore domains shows a net growth with an increment in the boundary slip, albeit this growth is very small [Figs. 9(c) and 9(d)]. With an increment in boundary slip, the growth in velocity tends to focus in the vicinity of pore throats, which results in a small growth in the net friction drag offered by the entire pore domain [Fig. 9(c)].

Likewise, a net growth in the form drag ($\mathrm{F_N}$) is found from the tortuous pores [Figs. 9(a) and 9(b)]. While the magnitude of form drag is smaller than the magnitude of friction drag, the amount of growth in form drag due to an increment in boundary slip is larger than the amount of growth in friction drag. For example, the growth in form drag is $\sim$20% more than the growth in friction drag for a pore-throat size, $d = 10^{-6}$ m [Fig. 9(c)]. In the vicinity of the diverging part of pores, the streamlines diverge towards the widest section of pore-body, which is a result of local pressure dissipation balanced by

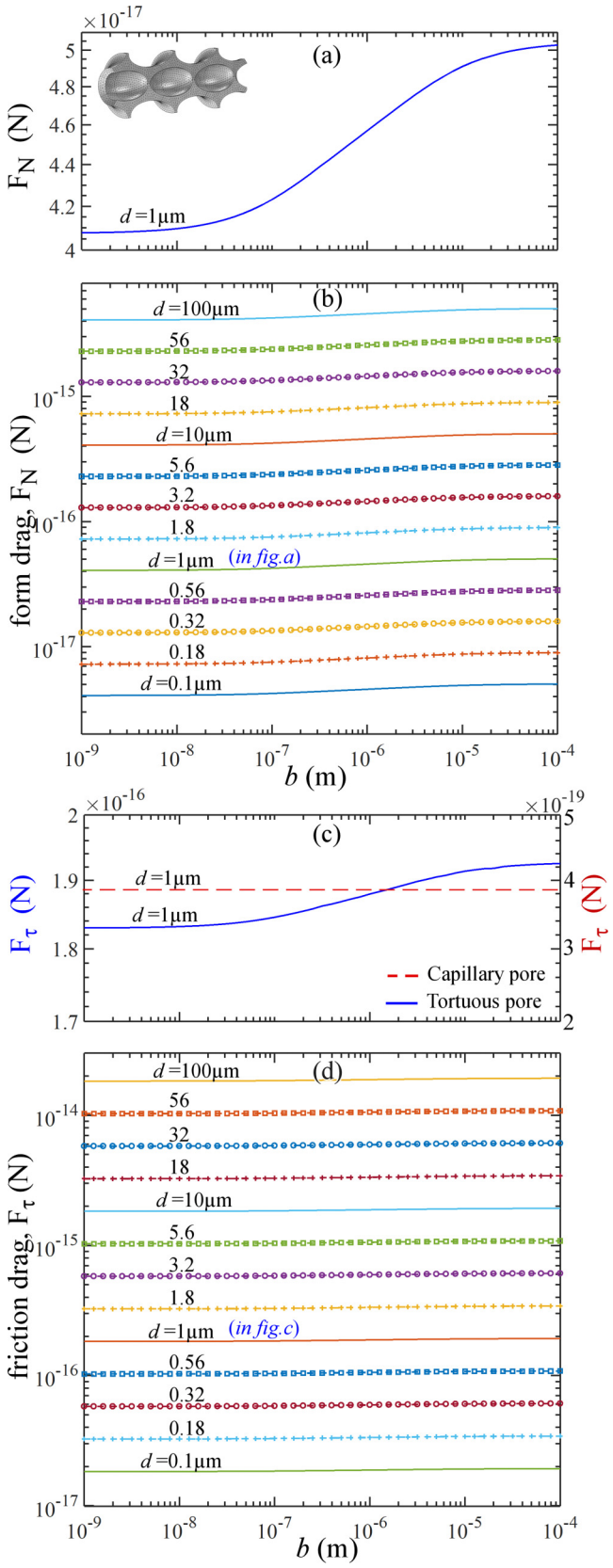


FIG. 9. Net changes in form drag, $F_N$(N) and friction drag, $F_\tau$(N) due to an increase in slip length $b$ at boundaries of tortuous pore domains of various pore-throat sizes $d$. Note, for a better display, (a) and (c) are semilog plots of forces also included in (b) and (d), respectively. Only (c) shows friction drag from the capillary pore.

the form drag on the boundary. And, with an increment in boundary slip, pressure dissipation expands towards the wider section of pore space, which leads to growth in the net amount of form drag. Using the integration of diverging streamlines from a geometry, similar to that considered in this study, Weissberg [46] derived the theoretical Eq. (12) to predict the pressure drop for a diverging pore geometry, and using Eq. (12), Sisan [49] derived the Eq. (13) to predict the related pressure drop due to the boundary slip. The occurrence of form drag in a diverging-converging geometry signifies additional pressure loss which is integral to theory, i.e., integral to Eq. (12), and growth in form drag with an increment in slip flows implies an expansion in pressure loss which gets manifested as the asymptote in the flow enhancement factors.

### B. Energy dissipation rate, $\varepsilon$

Viscous fluids are subject to loss of mechanical energy or energy dissipation due to viscous stresses in a flowing fluid. The energy dissipation or viscous losses are amplified when the fluid deviates from a straight flowing path, for example, when it flows around a structure or through a diverging-converging pore channel. Such a dissipation of energy is known to manifest as the permeability of porous media [51,52], and therefore, contribute to flow enhancement factors, $E_1$ and $E_2$. To examine if and how energy dissipation within pores may explain for the observed asymptote in the flow enhancement factor of diverging-converging tortuous pore geometries, energy dissipation rate ($\varepsilon$) is computed from pore domains with the no-slip and various slip boundary conditions as

$$\varepsilon = \boldsymbol{\tau} : \nabla \boldsymbol{u}, \tag{20}$$

where $\boldsymbol{\tau}$ is stress tensor and $\nabla \boldsymbol{u}$ is strain rate tensor.

#### *1. Capillary pores*

The linear pressure drop along the length of capillary pores results in a constant velocity profile, as such, the component of the velocity gradient orthogonal to the central line of the capillary pores remains constant. Likewise, the associated shear stress remains constant, both of which result in a constant amount of energy dissipation rate ($\varepsilon$) from the straight tube capillary pores (Fig. 10). Moreover, this energy dissipation rate ($\varepsilon$) is found to remain constant both in its distribution and its magnitude with an increase in boundary slip [Figs. 10(i)–10(l)].

#### *2. Diverging-converging tortuous pore*

The computed energy dissipation rate ($\varepsilon$) from the tortuous pore with the no-slip boundary condition shows that it is pronounced in the vicinity of pore throats (i.e., the narrow region around the label $d$ in Figs. 1(b) and 10(a), and diminishes away from pore throats towards the pore body [i.e., the wider region away from pore throats; Fig. 10(a)]. And, with an increase in boundary slip (i.e., when $b > 0$), the distribution of energy dissipation with a partial slip (i.e., when $b \ll d$) remains similar to the case of the no-slip boundary condition [Fig. 10(b)]. However, when boundary slip is on the order of the size of pore throats (i.e., when $b \sim d$), the distribution of

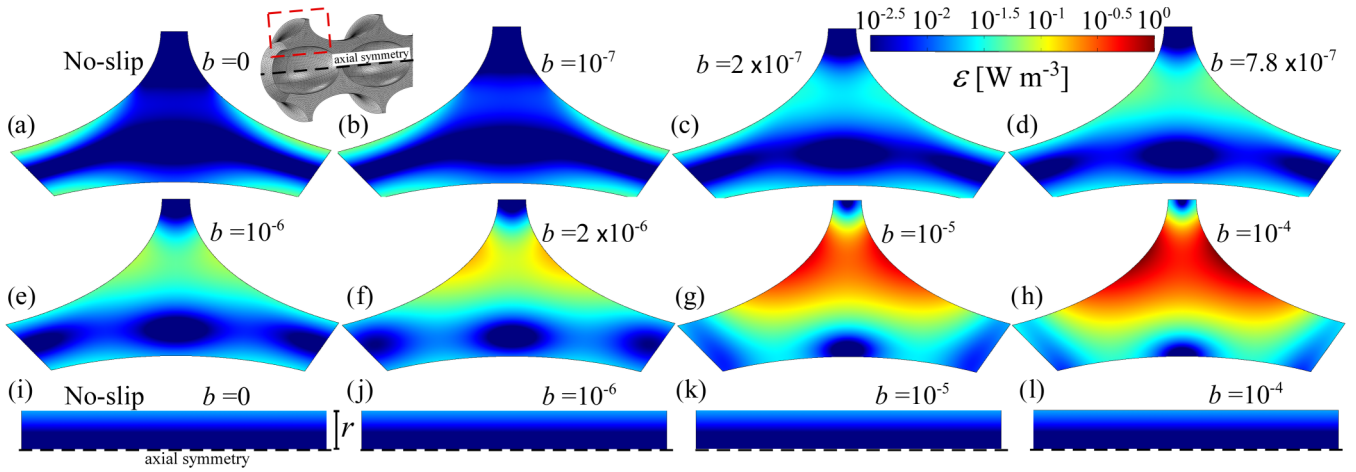


FIG. 10. (a)–(h) Energy dissipation rate $\varepsilon(\mathrm{W\,m^{-3}})$ showing an increase in energy dissipation from 2D half sections of tortuous pores of $d = 1$ μm (notice its location highlighted by dashed red rectangle in the inset), in comparison to no change in energy dissipation found from the capillary pore (i)–(l).

energy dissipation rate ($\varepsilon$) shows a focused increase in the region of the pore body [Figs. 10(c)–10(e)]. This transition in the distribution of energy dissipation rate ($\varepsilon$) from pore throat to pore body is found to get further magnified within the pore-body [Figs. 10(f) and 10(h)] for slip flow scenarios with a large boundary slip, i.e., when $b \gg d$.

The increase in energy dissipation due to an increase in boundary slip of a diverging-converging tortuous pore is manifested in the emergent Darcy flow behavior as a limitation to the flow enhancement marked by an asymptote in $E_1$ and $E_2$ [Figs. 6(b) and 8]. The straight tube capillary geometry offers no such change in energy dissipation due to an increase in boundary slip, and thus, contributes to an unlimited increase in flow enhancement [Figs. 6(a) and 7].

### C. Discussions

This study determines how pore geometry (i.e., diverging-converging tortuous pore vs capillary pore) plays a vital role in contributing to how variations in boundary slip of liquid flow, manifest in enhancing the flow or the permeability ($k$). It is found that with an increase in boundary slip from the no-slip condition, there is an unlimited linear increase in flow enhancement, e.g., as shown by the factors, $E_1$ and $E_2$ which can be attributed to the straight tube geometry of capillary pores. This unlimited nature of increase is, however, found to get limited within diverging-converging tortuous pore geometries. This limited increase is defined by an asymptote in the flow enhancement factors, $E_1$ and $E_2$. Similar asymptote in the flow enhancement factor or pressure loss has also been noted from computational studies on CNT [48], and investigations of end effects of nanochannels [49,53,54].

The physical mechanisms that are likely accountable for the asymptote in the flow enhancement of the diverging-converging tortuous pore geometry are examined using drag forces and energy dissipation rate. The nature of a straight tube in capillary pores results in a nil amount of form drag and a friction drag which remains unchanged with an increase in boundary slip. Similarly, the straight tube geometry of capillary pores offers no additional fluid deformation as such the energy dissipation is only due to the viscosity, and which remains unchanged with the boundary condition of either a no-slip or a boundary slip. Thus, the very nature of the straight tube geometry of capillary pores is found to offer no additional resistance to an increase in flow due to an increase in boundary slip, which manifests as the unlimited linear increase in the flow enhancement factors, $E_1$ and $E_2$.

In contrast, the diverging-converging tortuous pore geometry offers an increase in both the form drag and the friction drag related to an increase in boundary slip. Also, the energy dissipation rate is found to increases with an increase in the boundary slip. Thus, the very nature of diverging-converging tortuous pore geometry offers an increase in both the drag forces and energy dissipation rate, combined effect of which offer resistance to flow, and thus, limits or contribute to the asymptote in the flow enhancement factors, $E_1$ and $E_2$.

Finally, this study presents a set of theoretical models based on the works of Weissberg [46] and Sisan [49] that can be used to predict the flow enhancement factors, $E_1$ and $E_2$ both for a straight tube capillary geometry and a diverging-converging tortuous pore geometry as a function of boundary slip and spatial-scale of pore throats.

This study lays emphasis on how the geometry of pores plays a vital role in the emergent Darcy flow behavior as a result of boundary slip. The differences in the flow enhancement due to boundary slip are found to be over several orders of magnitude between when considering a more realistic, albeit synthetically designed, diverging-converging tortuous pore geometry in contrast to a straight tube capillary pore geometry. The majority of studies to date have utilized straight tube pore geometries for such investigations, for example, the usage of pore-network modeling, as such, our ability to predict pressure loss or flow enhancement or apparent permeability may be off by several orders of magnitude. These findings may be relevant to the applications of waste storage or energy recovery processes, e.g., waste fluid injection for storage or recovery of hydrocarbons from geologic reservoirs, and

likewise for many engineering applications, e.g., hydraulics in corrugated channels or design of CNT filters for desalinization purposes.

## V. SUMMARY

(a) Fundamental pore-scale investigations of how pore geometry and boundary slip conditions contribute to the emergent Darcy flow and flow enhancement factors, $E_1$ and $E_2$ are presented. Diverging-converging tortuous pores in contrast to straight tube capillary pores are designed to include a large variation in pore-throat sizes (i.e., $10^{-7}$ m to $10^{-4}$ m), found in geologic porous media. Computational fluid dynamics simulations are conducted for a sensitivity study to examine the effect of a large variation in boundary slip reported in the literature.

(b) Results show that with a systematic increase in boundary slip from the no-slip condition, pore-throat size, and pore geometry contribute to unique and systematic modifications with differences over several orders of magnitude in the emergent Darcy flow behavior and flow enhancement factors, $E_1$ and $E_2$. From straight tube capillary pores, flow enhancement factors, $E_1$ and $E_2$ are found to increase linearly in an unlimited manner with an increase in the boundary slip. In contrast, $E_1$ and $E_2$ from diverging-converging tortuous pores show a limited flow enhancement marked by an asymptote. The linear unlimited relationship from straight tube capillary pores indicate that the flow enhancement can be up to several orders of magnitude, whereas, the S-type characteristics or the asymptote, limits the maximum flow enhancement to $10^{1.23}$ or a factor of 17 in diverging-converging tortuous pores.

(c) This study finds that the flow enhancement due to boundary slip is always lower in a diverging-converging tortuous pore geometry relative to a straight tube capillary pore geometry. In addition, pore-throat sizes have a vital control over how a given slip length enhances effective flow or $E_1$ and $E_2$. Larger pore throats negligibly enhance flow, which, however, increasingly becomes significant for the micron size pore throats and smaller.

(d) The limited nature of flow enhancement marked by an asymptote for flows when boundary slip is proportional to the size of pore throats defines how slip flows manifest as an emergent Darcy flow behavior from a diverging-converging tortuous porous media, a finding which is consistent with previous studies on end effects of carbon nanotube membranes [48,49,53,54].

(e) The physical mechanisms which are likely accountable for the asymptote in the flow enhancement found from diverging-converging tortuous pores are examined using drag forces and energy dissipation rate. The straight tube geometry of capillary pores is found to offer a nil amount of form drag, and both the friction drag and the energy dissipation rate are found to be constant with changes in the boundary slip. Thus, capillary pores offer no change in resistance to flow which contributes to a linear or an unlimited increase in the flow enhancement. In contrast, the very nature of diverging-converging tortuous pore geometry offers an increase in drag forces and energy dissipation rate, i.e., an increase in resistance to flow, which limits or contributes to the asymptote in the flow enhancement.

(f) A set of theoretical models based on the works of Weissberg [46] and Sisan [49] are presented, which can be used to predict the flow enhancement factors, $E_1$ and $E_2$ both for a straight tube capillary geometry and a diverging-converging tortuous pore geometry as a function of boundary slip and spatial-scale.

(g) This study lays emphasis on how the geometry of pores plays a vital role in the emergent Darcy flow behavior as a result of the boundary slip. The differences in the flow enhancement between tortuous and capillary pore geometry are found to be over several orders of magnitude, which likely has direct implications for evaluating hydrocarbon recovery or pressure loss during fluid injection or recovery from low permeability reservoirs. Likewise, this study may bear implications for many other engineering applications, e.g., hydraulics in corrugated channels or design of carbon nanotube CNTmembranes for desalinization purposes.

## ACKNOWLEDGMENTS

The author thanks the Department of Geology, Kent State University, Ohio for providing the computational resources, and acknowledges a summer grant offered by the office of sponsored programs, Kent State University, Ohio.

[1] S. Whitaker, Transport. Porous Med. **1**, 3 (1986).
[2] S. P. Neuman, Acta Mech. **25**, 153 (1977).
[3] D. Lasseux and F. J. Valdés-Parada, Phys. Fluids **29**, 043303 (2017).
[4] A. Mehmani, M. Prodanovic, and F. Javadpour, Transport. Porous Med. **99**, 377 (2013).
[5] C. J. Landry, M. Prodanovic, and P. Eichhubl, Int. J. Coal Geol. **159**, 120 (2016).
[6] M. J. Blunt, B. Bijeljic, H. Dong, O. Gharbi, S. Iglauer, P. Mostaghimi, A. Paluszny, and C. Pentland, Adv. Water Resour. **51**, 197 (2013).
[7] X. F. Yang *et al.*., Adv. Water Resour. **95**, 176 (2016).
[8] B. Bijeljic, A. Raeini, P. Mostaghimi, and M. J. Blunt, Phys. Rev. E **87**, 013011 (2013).
[9] W. Deng, M. B. Cardenas, M. F. Kirk, S. J. Altman, and P. C. Bennett, Environ. Sci. Technol. **47**, 11092 (2013).
[10] M. T. Balhoff and K. E. Thompson, Aiche J. **50**, 3034 (2004).
[11] J. T. Fredrich, A. A. Digiovanni, and D. R. Noble, J. Geophys. Res-Sol. Ea. **111**, B03201 (2006).
[12] C. H. Arns, M. A. Knackstedt, W. V. Pinczewski, and W. B. Lindquist, Geophys. Res. Lett. **28**, 3361 (2001).
[13] M. J. Blunt, M. D. Jackson, M. Piri, and P. H. Valvatne, Adv. Water Resour. **25**, 1069, (2002).
[14] M. Oostrom *et al.*., Computat. Geosci. **20**, 857 (2016).
[15] E. Ruckenstein and C. S. Dunn, J. Colloid Interf. Sci. **59**, 135 (1977).
[16] P. Meakin and A. M. Tartakovsky, Rev. Geophys. **47**, Rg3002 (2009).

[17] P. A. Thompson and S. M. Troian, Nature (London) **389**, 360 (1997).
[18] C. Neto, D. R. Evans, E. Bonaccurso, H. J. Butt, and V. S. J. Craig, Rep. Prog. Phys. **68**, 2859 (2005).
[19] A. Afsharpoor and F. Javadpour, Fuel **180**, 580 (2016).
[20] R. S. Voronov, D. V. Papavassiliou, and L. L. Lee, Chem. Phys. Lett. **441**, 273 (2007).
[21] M. Majumder, N. Chopra, R. Andrews, and B. J. Hinds, Nature (London) **438**, 930 (2005).
[22] J. P. Rothstein, Annu. Rev. Fluid Mech. **42**, 89 (2010).
[23] N. V. Priezjev and S. M. Troian, J. Fluid Mech. **554**, 25 (2006).
[24] J. Ou, B. Perot, and J. P. Rothstein, Phys. Fluids **16**, 4635 (2004).
[25] A. Kucala, M. J. Martinez, Y. F. Wang, and D. R. Noble, Water Resour. Res. **53**, 7281 (2017).
[26] N. V. Priezjev, A. A. Darhuber, and S. M. Troian, Phys. Rev. E **71**, 041608 (2005).
[27] V. S. J. Craig, C. Neto, and D. R. M. Williams, Phys. Rev. Lett. **87**, 054504 (2001).
[28] E. Bonaccurso, M. Kappl, and H. J. Butt, Phys. Rev. Lett. **88**, 076103 (2002).
[29] P. Joseph and P. Tabeling, Phys. Rev. E **71**, 035303(R) (2005).
[30] K. Ahmad, X. Z. Zhao, and Y. L. Pan, Surf. Interface Anal. **49**, 594 (2017).
[31] A. Rios-Rodriguez, C. A. Palacios-Morales, E. Bernal, G. Ascanio, and J. P. Aguayo-Vallejo, J. Appl. Fluid Mech. **9**, 1035 (2016).
[32] E. Lauga and H. A. Stone, J. Fluid Mech. **489**, 55 (2003).
[33] C. Lee, C. H. Choi, and C. J. Kim, Exp. Fluids **57**, 176 (2016).
[34] C.-H. Choi and C.-J. Kim, Phys. Rev. Lett. **96**, 066001 (2006).
[35] D. I. Konopinski, S. Hudziak, R. M. Morgan, P. A. Bull, and A. J. Kenyon, Forensic Sci. Int. **223**, 245 (2012).
[36] S. Iglauer, C. H. Pentland, and A. Busch, Water Resour. Res. **51**, 729 (2015).
[37] K. Chaudhary, E. J. Guiltinan, M. B. Cardenas, J. A. Maisano, R. A. Ketcham, and P. C. Bennett, Geochem. Geophy. Geosy. **16**, 2858 (2015).
[38] S. Al-Anssari, A. Barifcani, S. B. Wang, L. Maxim, and S. Iglauer, J. Colloid Interf. Sci. **461**, 435 (2016).
[39] P. Chiquet, D. Broseta, and S. Thibeau, Geofluids **7**, 112 (2007).
[40] P. H. Nelson, AAPG Bull. **93**, 329 (2009).
[41] P. W. J. Glover and E. Walker, Geophysics **74**, E17 (2009).
[42] A. S. Al-Kharusi and M. J. Blunt, J. Pet. Sci. Eng. **56**, 219 (2007).
[43] K. Chaudhary, M. B. Cardenas, W. Deng, and P. C. Bennett, Geophys. Res. Lett. **38**, L24405 (2011).
[44] M. B. Cardenas, Geophys. Res. Lett. **35**, L18402 (2008).
[45] P. K. Panigrahi and M. Asfer, in *Encyclopedia of Microfluidics and Nanofluidics*, edited by D. Li (Springer US, Boston, MA, 2008), pp. 140.
[46] H. L. Weissberg, Phys. Fluids **5**, 1033 (1962).
[47] R. Roscoe, Philos. Mag. **40**, 338 (1949).
[48] A. Popadic, J. H. Walther, P. Koumoutsakos, and M. Praprotnik, New J. Phys. **16**, 082001 (2014).
[49] T. B. Sisan and S. Lichter, Microfluid Nanofluid **11**, 787 (2011).
[50] K. Chaudhary, M. B. Cardenas, W. Deng, and P. C. Bennett, Water Resour. Res. **49**, 1149 (2013).
[51] M. Pilotti, S. Succi, and G. Menduni, Europhys. Lett. **60**, 72 (2002).
[52] R. W. Nelson, Soc. Pet. Eng. J. **8**, 33 (1968).
[53] J. H. Walther, K. Ritos, E. R. Cruz-Chu, C. M. Megaridis, and P. Koumoutsakos, Nano Lett. **13**, 1910 (2013).
[54] J. L. Zhao, Q. J. Kang, J. Yao, L. Zhang, Z. Li, Y. F. Yang, and H. Sun, Int. J. Heat Mass Tran. **125**, 1131 (2018).